Nonlinear rotation of spin-orbit coupled states in hollow ring-core fibers

SAI KANTH DACHA[1,*], WENQI ZHU[2], AMIT AGRAWAL[2], KENNETH J. RITTER[3], AND THOMAS E. MURPHY[1]

[1] *Institute for Research in Electronics and Applied Physics (IREAP), University of Maryland, College Park, Maryland 20742, USA*
[2] *National Institute of Standards and Technology (NIST), Gaithersburg, Maryland 20878, USA*
[3] *Laboratory for Physical Sciences (LPS), College Park, Maryland 20740, USA*
[*] *sdacha@umd.edu*
https://photonics.umd.edu/

Abstract: We experimentally demonstrate that when two spin-orbit coupled orbital angular momentum (OAM) modes of opposite topological charge co-propagate in the Kerr nonlinear regime in a hollow ring-core optical fiber, the vectorial mode superposition exhibits a unique power-dependent rotation effect. This effect is analogous to nonlinear polarization rotation in single-mode fibers, however, the added spatial dimension produces a visually observable rotation of the spatial pattern emerging from the fiber when imaged through a linear polarizer. A dielectric metasurface q-plate was designed and fabricated to excite the desired mode combination in a hollow ring-core fiber that supports stable propagation of OAM modes. The observed spatial patterns show strong agreement with numerical simulations of the vector coupled nonlinear Schrödinger equations. These results constitute the first measurements of what can be described as the spin-orbit coupled generalization of the nonlinear polarization rotation effect.

1. Introduction

Vortex beams or modes carrying orbital angular momentum (OAM) have a characteristic spiral phase distribution $e^{il\phi}$, where l is an integer and is referred to as the topological charge of the beam. Each photon in such a beam possesses an orbital angular momentum equal to $l\hbar$ [1]. Vortex beams have recently gained significant attention due to their wide-ranging applications in areas such as optical tweezers and particle trapping [2–4], classical [5–8], quantum [9–11] communication, optical metrology [12, 13] and quantum optics [14–16]. In the context of optical fibers, driven by an interest in spatially multiplexed communication systems, novel fiber designs with tailored refractive index profiles have recently been demonstrated to support stable linear propagation of OAM-carrying modes [17, 18].

Simultaneously, there has also been growing interest in nonlinear optical effects occurring in multimode fibers (MMFs). Similar to the case of single-mode fibers (SMFs), nonlinear impairments are expected to play an important role in MMF-based communication systems [19–21]. Numerous spatiotemporal nonlinear phenomena have been observed and studied in conventional MMFs over the past few years, including Kerr-induced beam self-cleanup [22, 23], the occurrence of multimode solitons [24], supercontinuum generation [25, 26] and spatiotemporal modulation instability [27].

Although there have been many studies of linear propagation of OAM modes in fibers, there have been relatively few that focus on nonlinear propagation effects [28]. As with conventional single- and multi- mode fibers, nonlinear effects in OAM-carrying fibers would be of fundamental importance from a telecommunications perspective. Given the aforementioned broad interest in OAM beams for applications ranging from nanoparticle manipulation in physical and biological systems to optical metrology and fundamental physics, nonlinear effects involving OAM-carrying fiber modes could unlock novel ways of controlling the light beam for a wide variety of applications. For example, octave-wide supercontinuum generation has recently been reported in ring-core fibers where the entire supercontinuum resides in a single spin-orbit coupled mode, enabling applications in super-resolution nanoscopy [28, 29]. More recently, Liu et al. have taken advantage of conservation of OAM to demonstrate controlled parametric four-wave mixing (FWM), paving way for light sources capable of generating OAM-carrying nanosecond pulses at user-specified wavelengths [30]. Here, we report, for the first time to the best of our knowledge, the effects of self-phase modulation (SPM) and intermodal cross-phase modulation (XPM) among OAM modes in a fiber, which produces a unique power-dependent spatial mode rotation.

In this work, we use a hollow ring-core fiber (RCF) that has a refractive index profile tailored to support stable linear propagation of OAM modes [18]. The large index step arising from the presence of a central air core results in the spin (i.e., polarization) and orbital degrees of freedom becoming coupled. This is the so called spin-orbit coupling effect, where propagation constants and group velocities of modes of the same topological charge l depend on whether the spin angular momentum (SAM; i.e., polarization) and OAM are aligned [31–33]. Modes for which SAM and OAM are aligned are referred to as spin-orbit aligned (SO_a) modes, while those for which SAM and OAM are of opposite helicities are referred to as the spin-orbit anti-aligned (SO_{aa}) modes. In this work, we consider the nonlinear evolution of a superposition of the degenerate SO_{aa} modes of topological charge $|l| = 10$. As we illustrate below, such a superposition consists of a spatially-varying elliptical state of polarization (SOP).

There are several methods for generating free-space OAM beams, and they can be grouped into two broad categories. The first includes methods that utilize a phase discontinuity to generate OAM beams from Gaussian beams, such as spiral phase plates [34], mode converters [35] and forked gratings [36]. These techniques are polarization insensitive, and therefore do not couple the OAM of the generated beam to its SAM. The second group includes methods that couple the OAM with the beam's SAM, and are usually based on the Pancharatnam-Berry (PB) geometric phase. Examples of such devices include the q-plate [37], J-plate [38] and p-plate [39]. Exciting a mode combination in the fiber that consists of a spatially-varying elliptical SOP requires a beam-shaping technique that is capable of coupling SAM and OAM. Because the modes of interest have the same $|l|$ value, the q-plate is an ideal choice.

Q-plates are commonly fabricated using liquid crystals (LCs), which are spatially oriented using the photo-alignment method, self-assembly or circular rubbing [40]. More recently, q-plates based on dielectric nanostructured metasurfaces have been demonstrated [41]. In contrast to LC devices, metasurface devices offer the capability to structure a light beam at the sub-wavelength scale, and are capable of simultaneous polarization and phase control. Furthermore, LC devices are prone to damage under high intensity illumination that is often required in nonlinear optical experiments. In this work, we design and fabricate a metasurface q-plate that is capable of exciting a controllable combination of the $|l| = 10$ SO_{aa} modes.

In the following, by employing the metasurface q-plate, we first demonstrate tunable excitation of the $l = \pm 10$ SO_{aa} modes of a hollow ring-core fiber. We tune the relative amplitudes of the two modes by simply varying the polarization of the input free-space Gaussian beam using a quarter-wave plate. For the general case of unequal amplitudes of the two modes, because the two modes have opposite signs of topological charges as well as opposite helicities of polarization, the mode superposition consists of a spatially-varying elliptical SOP. The intensity profile of this mode composition remains a doughnut, however, upon imaging the fiber output through a linear polarizer, the spatially-varying SOP is evident by the appearance of $2|l| = 20$ lobes.

When the two modes have unequal amplitudes, as the input power is increased, they acquire different nonlinear phase shifts arising from SPM and XPM. This results in a spatial interference pattern that is power-dependent. We demonstrate using experimental observations, numerical simulation and theoretical analysis that this spin-orbit coupled mode superposition exhibits a power-dependent rotation of its vectorial spatial pattern analogous to the nonlinear polarization rotation (NPR) effect occurring in SMFs.

2. Theory and Modeling

2.1. Spin-orbit coupled modes

The large index step encountered by the electromagnetic field at the air-glass interface within the core layer leads to a coupling of the polarization and phase properties. This spin-orbit coupling results in the linear propagation properties of a mode with a given OAM order l to depend on its SOP. Put differently, the degeneracy between the SO_a and SO_{aa} mode groups is lifted [33]. Note that the term "spin-orbit coupled state" describes any superposition of modes in such fibers. Here, we consider a general superposition of the degenerate SO_{aa} modes for $|l| = 10$. We will denote these modes as ${SO_{aa}}^{+10}$ and ${SO_{aa}}^{-10}$, where the superscript ± 10 denotes the topological charge of the modes. The OAM modes can be expressed in terms of the hybrid EH fiber modes as follows: ${SO_{aa}}^{\pm l} = (EH^{e}_{l-1} \pm i EH^{o}_{l-1})/\sqrt{2}$, where the superscripts e and o refer to the even and odd modes.

Fig. 1(a) shows an optical micrograph of the hollow RCF used in this work alongside its refractive index (RI) profile. The intensity, phase and polarization profiles of the two SO_{aa} modes are also shown. Note that each of the modes consists of spatially uniform circular states of polarization, and that the helicities of the polarization and OAM are opposite to each other.

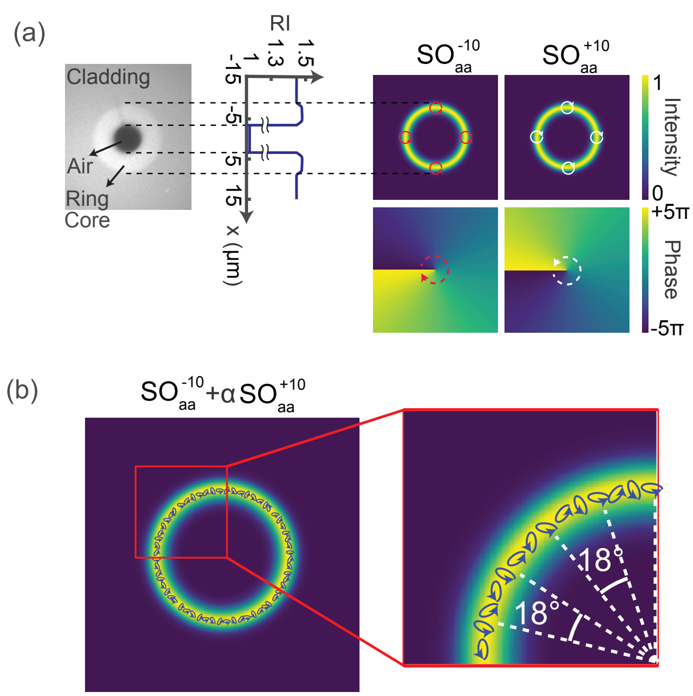

Fig. 1. Modes of a hollow ring-core fiber. (a) Optical micrograph of the cross-section of hollow RCF, overlaid with the refractive index profile. The intensity, polarization and phase profiles of the $l = \pm 10$ SO_{aa} modes are shown. Note that the modes have opposite helicities of polarization and phase. (b) A superposition of the two modes with $\alpha \neq 1$ results in a spatially varying elliptical state of polarization. The ellipticity at each point is the same, and is determined by the relative amplitudes, while the orientation of the ellipses rotates 2π every $360° /(2|l|) = 18°$.

Fig. 1(b) shows a general superposition of the two modes. For $\alpha \neq 1$, the superposition produces a spatially non-uniform elliptical SOP. The orientation of the local polarization ellipse undergoes a $2|l| = 20$-fold rotation along the azimuthal direction.

2.2. Analogy with nonlinear polarization rotation in SMFs

Nonlinear evolution of this spin-orbit coupled state can be studied by using the coupled nonlinear Schrödinger equations (NLSEs). It is instructive to first write down the NLSEs in the hybrid mode basis. Denoting E_1 and E_2 as the slowly-varying complex pulse envelopes of the EH^e and EH^o modes, the NLSEs in the hybrid mode basis are given by [42]:

$$\frac{\partial E_1}{\partial z} = i\gamma \left(|E_1|^2 E_1 + \frac{2}{3}|E_2|^2 E_1 + \frac{1}{3} E_2^2 E_1^* \right) \tag{1a}$$

$$\frac{\partial E_2}{\partial z} = i\gamma \left(|E_2|^2 E_2 + \frac{2}{3}|E_1|^2 E_2 + \frac{1}{3} E_1^2 E_2^* \right) \tag{1b}$$

where γ denotes the SPM coefficient. Upon transforming Eqs. (1a) and (1b) from the hybrid mode basis to the OAM mode basis, we obtain:

$$\frac{\partial V^+}{\partial z} = \frac{2i}{3}\gamma \left(|V^+|^2 + 2|V^-|^2 \right) V^+ \tag{2a}$$

$$\frac{\partial V^-}{\partial z} = \frac{2i}{3}\gamma \left(|V^-|^2 + 2|V^+|^2 \right) V^- \tag{2b}$$

where $V^{\pm}$ denote the slowly-varying complex pulse envelopes of the ${\mathrm{SO_{aa}}}^{\pm 10}$ modes respectively. As one can see from the right hand side of Eqs. (2a) and (2b), SPM and intermodal XPM are the only surviving nonlinear products in the coupled NLSEs in the OAM mode basis.

Note that the NLSEs (1a), (1b) and (2a), (2b) are identical to the well-known coupled NLSEs in the polarization basis in isotropic SMFs [43]. NLSEs in the hybrid mode basis resemble those written in the x-y polarization basis in SMFs, while the NLSEs in OAM mode basis resemble those in the circular polarization basis. This makes for an effective analogy with which to better visualize the nonlinear evolution of the spin-orbit coupled state described above in RCFs.

Recall that in the case of nonlinearly interacting polarization modes in isotropic SMFs, for an input elliptical SOP, NLSEs expressed in the circular polarization basis point to a dependence of the phase difference between the left and right circular polarizations (LCP and RCP) on the input power and fiber length. For a fixed fiber length, as a result of this power-dependent phase difference between LCP and RCP, the orientation of the resulting elliptical SOP also acquires a power dependence. Equivalently, in the Poincaré sphere representation, the Stokes vector rotates about the S_3-axis with an angular velocity that is proportional to the nonlinear coupling between the optical fields in the left and right circular polarizations. This is the well-known self-induced ellipse rotation, also often referred to as nonlinear polarization rotation (NPR) [43], which is now widely employed in femtosecond mode-locked fiber lasers.

In the case of spin-orbit coupled modes, a similar power-dependent evolution is expected to occur. As shown in Fig. 1(b), a general superposition of the degenerate $\mathrm{SO_{aa}}$ modes with unequal mode amplitudes leads to a spatially-varying elliptical SOP. The ellipticity of the polarization ellipse at each spatial location is determined by the relative amplitudes of the modes, whereas the orientation of the local ellipse varies along the azimuthal direction. The overall orientation of the pattern is determined by the phase difference between the overlapping OAM modes. In the presence of SPM and intermodal XPM as described in Eqs. (2a), (2b), the two modes acquire a power-dependent phase difference. This leads to a power-dependent rotation of the overall spatial polarization pattern. Equivalently, the polarization ellipse at one spatial location rotates as a function of input power.

While nonlinear polarization rotation is a useful analogy, it is not directly equivalent to the effect reported here, which depends upon the existence of a spatially varying phase provided by the OAM modes. Furthermore, on a practical level, occurrence of this phenomenon relies upon the spin-orbit coupling effect, in the absence of which the SO_a and SO_{aa} mode groups would become degenerate with each other. As a result, attempting to couple into one of the mode groups would inevitably also excite the other mode group, which would then alter the dynamics of the nonlinear interaction. As a result, this phenomenon is to be interpreted as a generalization of SMF-based nonlinear polarization rotation to the multimoded, spin-orbit coupled context in OAM fibers.

2.3. Numerical simulation

We verify the analytical arguments made above using numerical simulations. The spatial modes of the fiber were computed using an open source finite element mode solver reported in [44]. The nonlinear evolution of the mode superposition of interest was studied by numerically solving the coupled NLSEs Eqs. (2a), (2b) using the split-step Fourier method (SSFM).

The images on the left hand side of Supplementary Video 1 show the numerically simulated spatiotemporal evolution of a Gaussian (in time) pulse coupled into the mode superposition described above, for a sufficiently high input peak power. Because the instantaneous power varies as a function of time within one pulse duration, the instantaneous orientation of the spatial polarization pattern also rotates about the fiber axis as a function of time. Equivalently, the local polarization ellipse at each point in space rotates as a function of time.

This effect is more easily observable experimentally upon imaging it through a linear polarizer. The insertion of a linear polarizer causes the appearance of $2|l| = 20$ lobes in the intensity pattern. Because of the temporal rotation of the spatial polarization pattern, the resulting lobe pattern also rotates as a function of time. This is shown on the right hand side of Supplementary Video 1.

Furthermore, upon increasing the input peak power, the net rotation attained by the instantaneous lobe pattern at the pulse peak also increases. The change in net rotation at the pulse peak as a function of input peak power can be characterized by simply measuring the rotation, as a function of input peak power, of the *time-averaged* intensity pattern imaged using a slow camera. Although the instantaneous orientation of the lobe pattern varies within one pulse duration, the orientation at the pulse peak is easily visible even in a time-averaged image as it is the brightest part of the pulse. Simulation results of this are shown in Supplementary Video 2. As the input peak power is increased, the time-averaged lobe intensity pattern exhibits a power-dependent rotation. The blurring of the pattern observed at higher input powers in the simulated time-averaged images is a result of the fact that the instantaneous orientation of the lobe pattern changes within the duration of the pulse. It is worth noting that the blurring, i.e., a reduction in the “contrast” of the lobes with an increase in input power, is analogous to the apparent nonlinear depolarization effect observed as a result of temporal averaging of non-square pulses in the case of NPR in SMFs.

3. Experiment

The nonlinear effect described above was verified experimentally by first demonstrating tunable excitation of the $l = \pm 10$ SO_{aa} modes using a transmissive dielectric metasurface q-plate. Fig. 2(a) shows a schematic of the working of a q-plate of a given order q. For a Gaussian (i.e., $l = 0$) input beam with an elliptical SOP, the output produced consists of a mixture of $l = +2q$, $l = -2q$ and $l = 0$ beams. Fig. 2(b) shows an illustration of each unit cell, consisting of a high aspect-ratio amorphous Si (a-Si) nanofin structure of rectangular cross-section that functions as a half-wave plate (HWP) at $\lambda_0 = 1064$ nm [45]. The fast axis orientation of the nanofin HWP is determined by the design equation $\Theta = 2|q|\phi = |l|\phi$, where ϕ is the angular coordinate of the unit cell relative to the center of the metasurface. Fig. 2(c) illustrates the spatial arrangement of these nanofin HWP unit cells. Each nanofin is nominally of length: 272 nm, width: 104 nm, and height: 760 nm. The nominal separation between adjacent unit cells is 400 nm. The q-plate phase profile imparted on an incoming optical beam by the nanofin pattern is expressed in polar coordinates as $\alpha(r, \phi) = \Theta(r, \phi)/2 = |q|\phi$, according to the geometric Pancharatnam-Berry (PB) phase [46]. The metasurface design based on the PB phase naturally provides opposite topological charge numbers for orthogonal circular polarization states.

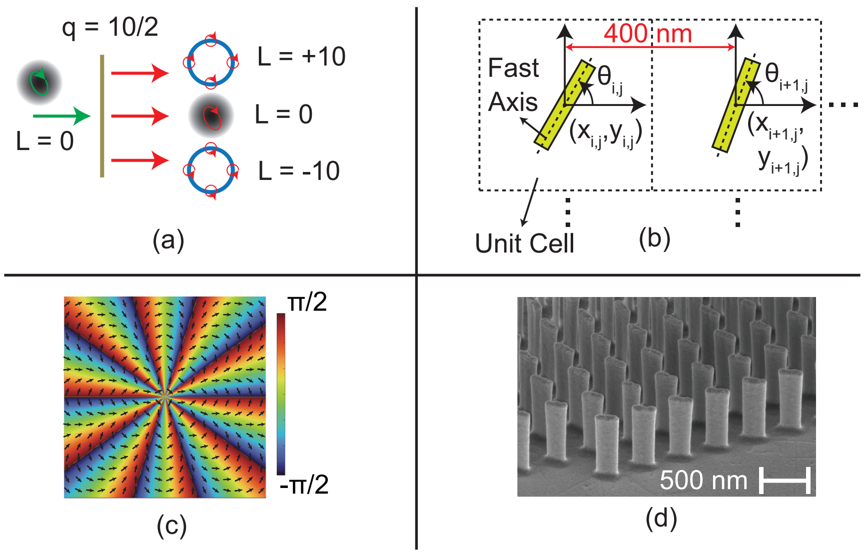

Fig. 2. Tunable excitation of $l = \pm 10$ modes using a metasurface q-plate. (a) Schematic of a q-plate of order $q = |l|/2 = 10/2$. For an input Gaussian beam for some elliptical state of polarization, the output consists of a mixture of the $l = \pm 10$ free-space OAM beams as well as an unconverted Gaussian remnant. (b) Illustration showing a unit-cell of the metasurface q-plate, consisting of an amorphous Si nanofin that acts as a half-wave plate, with fast-axis orientation $\theta_{i,j}$ and spatial position $(x_{i,j}, y_{i,j})$ on the spatial grid. The separation between adjacent unit cells is 400 nm. (c) Colormap overlaid with a quiver plot showing the 2-dimensional spatial distribution of unit cell fast axes orientations on the metasurface. The orientation of the fast axes is given by $\Theta = |l|\phi$ for $|l| = 10$, where ϕ is the angular coordinate. (d) Scanning electron micrograph of the fabricated metasurface q-plate showing individual nanofins

The metasurface optics is fabricated by depositing a layer of 760 nm thick a-Si on a 500 μm thick fused silica wafer using plasma enhanced chemical vapor deposition (PECVD). A 300 nm thick layer of high-resolution positive tone electron beam resist followed by a 20 nm thick layer of anti-charging conductive polymer are spin-coated onto the a-Si film. A 100 keV electron beam lithography system is used to expose the nanopillar pattern, followed by conductive polymer removal with deionized water at room temperature, and resist development with hexyl acetate at 4°C. The developed pattern in the resist layer is transferred to an electron-beam-evaporated 70 nm thick Al_2O_3 layer using the lift-off technique. By using the patterned Al_2O_3 layer as an etch mask, inductively-coupled-plasma reactive ion etching (ICP-RIE, gas mixture: SF_6 and C_4F_8; ICP power: 1750 W; radio frequency power: 15 W) is performed to etch the underlying a-Si layer at 15 °C, to create high-aspect-ratio a-Si nanopillars. The metasurface optics fabrication is finalized by soaking the wafer in a mixture of hydrogen peroxide and ammonium hydroxide solutions (80 °C for 30 min) to remove the Al_2O_3 etch mask and any etch residue.

Fig. 3 shows the experimental schematic used to characterize nonlinear rotation of the mode superposition described above. The Nd:YAG microchip laser used in this work produces optical pulses with a temporal full-width-at-half-maximum (FWHM) duration of 720 ps at $\lambda = 1064$ nm with a repetition rate of 1 kHz. The beam has a Gaussian spatial profile and is linearly polarized. A combination of a HWP and a polarization beam splitter (PBS) is employed to adjust the power transmitted through to the metasurface q-plate. A quarter-wave plate (QWP) is used to tune the SOP of the Gaussian beam before it is incident on the metasurface q-plate described above. The free-space output beam consists of a combination of $l = \pm 10$ and $l = 0$ beams. The conversion efficiency of the q-plate, i.e., the ratio of power in the $l \neq 0$ and $l = 0$ parts of the beam, is measured to be ≈ 20 %. Higher spin-to-orbital conversion efficiencies of the metasurfaces exceeding that achieved in the experiments presented here is expected through further design and nanofabrication improvements [47]. The relative powers in the $l = +10$ and $l = -10$ parts of the beam are tuned by adjusting the input SOP using the QWP. This beam is then focused down onto the input end face of a cleaved hollow RCF (Fig. 1). It is important to note that the non-guiding air core of the RCF acts as an effective spatial filter for the $l = 0$ part of the q-plate output, thereby only coupling into the $l = \pm 10$ modes in the fiber. This is because of the well-known property of Laguerre-Gaussian (LG) free-space beams that for a given lens of focal length f, beams of different l values focus to different spot sizes [48]. The focal length f of the lens used was chosen such that the resulting spot size of the $l = \pm 10$ part of the beam ≈ 17 μm, roughly matching the guiding core diameter of the hollow RCF, whereas the spot size of the $l = 0$ beam was < 3 μm, much smaller than the diameter of the air core. Characterization measurements described below show that the power coupled into other modes is negligible, and that tunable excitation of the ${SO_{aa}}^{\pm 10}$ modes is achieved.

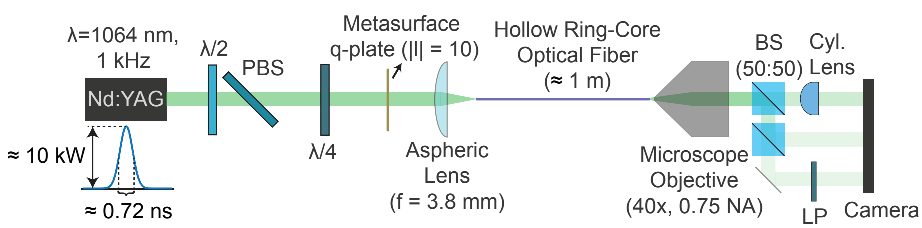

Fig. 3. Schematic of the experimental setup constructed to study nonlinear rotation of spin-orbit coupled states in hollow RCFs.

The beam emerging from the fiber is magnified using a infinity-corrected microscope objective of 40x magnification and a numerical aperture (NA) of 0.75 before it is imaged through polarization and mode-converting optics. We employ a linear polarizer to image the output beam to observe the $2|l| = 20$ lobe pattern, and a cylindrical lens to convert the Laguerre-Gaussian beam, corresponding to the fiber OAM modes, to Hermite-Gaussian (HG) beam that makes it possible to examine the OAM mode content in the fiber [35]. For the imaging mechanism, although we previously demonstrated a method to resolve the near field output intensity of MMFs with a sub-nanosecond temporal resolution [49], such a near field method does not allow for the insertion of free-space polarization optics. Other similar techniques [50] could be viable, but time-averaged methods such as using a slow imaging camera prove sufficient for characterizing the phenomenon of interest here. The time-averaged images acquired are then processed and analyzed, and the results are compared with numerical simulations described above.

4. Results and Discussion

4.1. Tunable excitation of $l = \pm 10$ SO_{aa} modes

As the SOP of the Gaussian beam incident on the q-plate is varied, the relative amplitudes of the $l = \pm 10$ LG beams also vary; this is the essential functionality of a q-plate. The metasurface design based on the PB phase provides opposite signed topological charges for orthogonal circular polarization states, thereby exciting only the SO_{aa} modes in the fiber. Furthermore, the aforementioned spin-orbit coupling effect occurring in these fibers provide a sufficient effective index separation between the SO_{aa} and SO_a mode groups, which prevents unintentional excitation of the SO_a modes via linear coupling in the fiber.

Fig. 4 shows how different linear combinations of the $l = \pm 10$ SO_{aa} modes of the fiber can be excited depending on the orientation of the input QWP. The OAM mode content in the fiber is revealed by imaging the fiber output through a cylindrical lens that acts as a mode converter. For an input SOP that is LCP(RCP), the q-plate produces an output OAM beam that is LCP (RCP) and has a topological charge of $l = +10$ ($l = -10$), thereby exciting only the $l = +10$ ($l = -10$) SO_{aa} mode in the fiber. This is evidenced by the appearance of a Hermite-Gaussian mode pattern that has a positive (negative) slope when imaged using a cylindrical lens, as shown in the top left (right) image in Fig. 4. The $|l|$ value of this beam is confirmed to be 10 by counting the number of dark fringes in the pattern. For an input SOP that is elliptical or linear, the q-plate output contains a mixture of both $l = \pm 10$ beams, each with polarization helicities opposite to their OAM phase helicities. Such a beam excites an admixture of the two $l = \pm 10$ SO_{aa} modes in the fiber, producing orthogonal HG mode patterns indicating the presence of topological charges of opposite signs. The number of dark fringes in each of the orthogonal arms is verified to be 10. The special case of a linear input SOP excites the two SO_{aa} modes with equal amplitudes, which can be equivalently described as the excitation of a pure EH mode.

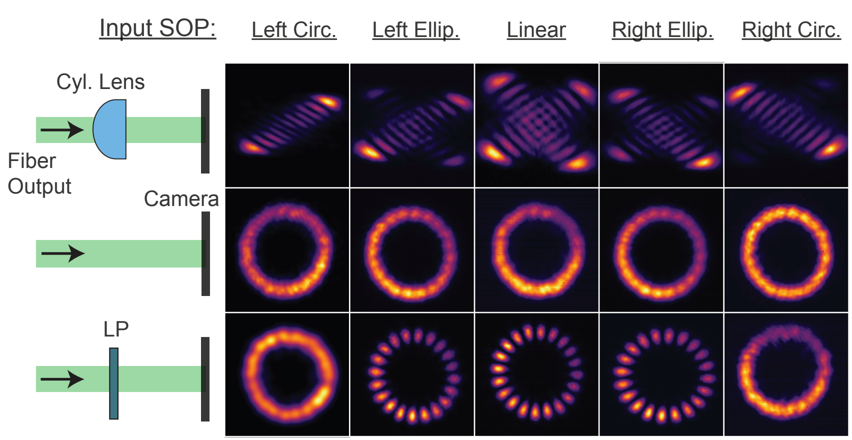

Fig. 4. Demonstration of tunable excitation of $l = \pm 10$ SO_{aa} modes in a hollow RCF using a metasurface q-plate: experimental images. The beam exiting the fiber is imaged at different input SOPs. (Top) A cylindrical lens is used to convert the LG beam emerging from the fiber to the HG basis, to reveal the OAM mode content in the fiber. (Middle) Polarization-insensitive measurement of the intenstity pattern of the output beam. (Bottom) When imaged through a linear polarizer, $2|l| = 20$ lobes appear for all input SOPs except for LCP and RCP, each of which excite purely one OAM mode.

For all input SOPs, the intensity profile of the output beam always has a ring shape, characteristic of OAM-carrying modes and their superpositions. When imaged through a linear polarizer, however, only the cases of LCP and RCP retain the ring shape in their intensity profiles. This once again demonstrates in both of these cases, only one OAM mode with a spatially uniform SOP is excited. For an input SOP that is elliptical, we observe $2|l| = 20$ lobes in the measured intensity pattern. This arises from the fact that the mode superposition for such an input consists of a spatially-varying elliptical SOP, as indicated in Fig. 1(b). For the case of a linear input SOP, the excited EH mode has a spatially-varying linear SOP, which also results in the appearance of the lobe pattern. This demonstrates that by tuning the SOP of the Gaussian beam incident on the metasurface q-plate, the $SO_{aa}{}^{\pm 10}$ mode content in the fiber can be adjusted.

It is also worth noting that the absence of any HG mode pattern corresponding to $l = 0$, as can be seen from the top row of Fig. 4, shows that the unconverted $l = 0$ part of the beam exiting the metasurface q-plate is not guided in the fiber, as predicted.

4.2. Power-dependent rotation of time-averaged lobe intensity patterns

As described in Section 2, for an unequal mixture of the two modes, as the input power is increased, the modes undergo SPM and intermodal XPM, leading to a time-varying orientation of the lobe pattern within the duration of a pulse when imaged through a linear polarizer. However, this power-dependent rotation is also readily verified by observing the change in the time-averaged intensity pattern as the input power is increased. Fig. 5 shows numerically simulated and experimentally measured time-averaged images for two configurations of the input QWP. The first QWP configuration results in a right elliptical SOP of the Gaussian beam incident on the q-plate, and excites a mode combination with the $l = -10$ SO_{aa} mode being the dominant one. The second QWP configuration excites a dominant $l = +10$ SO_{aa} mode combination.

Fig. 5 also shows numerically simulated and experimentally measured images of the time-averaged intensity pattern imaged through a linear polarizer at various input peak powers. The radial tick marks overlaid on the images show the location of the intensity lobes at low power and the degree (and direction) of power-dependent rotation. For the experimental images, the pattern rotation was calculated using Fourier image processing, as described below. As the input power is increased, the lobe patterns are no longer aligned with that at low input power, and the amount of rotation increases with an increase in input power, indicating the nonlinear origin of this effect.

The sense of rotation depends on the handedness of the input polarization: the dominant $l = -10$ case is counter-clockwise, whereas the dominant $l = +10$ case rotates clockwise, as the input power increases. This effect is explained by observing from Eqs. (2a), (2b) that the nonlinear phases acquired by each of the modes depends upon the power distribution in the two modes. For a dominant $l = -10$ configuration, the $l = +10$ mode acquires more nonlinear phase than the $l = -10$ mode due to intermodal XPM, and vice versa. Because the orientation of the resulting lobes is determined by the phase difference between the two modes, the two cases result in opposite senses of rotation.

Fig. 5 also shows a blurring of the lobe pattern with power, i.e., a reduction in the contrast at higher input powers, for both simulations and experimental images. This a result of the time averaging process, and confirms indirectly that the lobe pattern undergoes a time-dependent rotation within one pulse duration, as predicted by numerical simulations shown in Supplementary Video 1.

The rotation and blurring of these lobe patterns is strikingly apparent when the time-averaged images recorded at various input power levels are played in succession as a movie. Supplementary Video 2 shows numerically simulated time-averaged images for the case of dominant $l = -10$ mode. Supplementary Video 3(4) shows experimentally obtained images for the dominant $l = -10(l = +10)$ case. Notice from Supplementary Videos 3 and 4 the increase in rotation as well as reduction in lobe contrast with an increase in input peak power. Notice also that the dominant $l = -10$ and dominant $l = +10$ cases show opposite senses of rotation. This is in

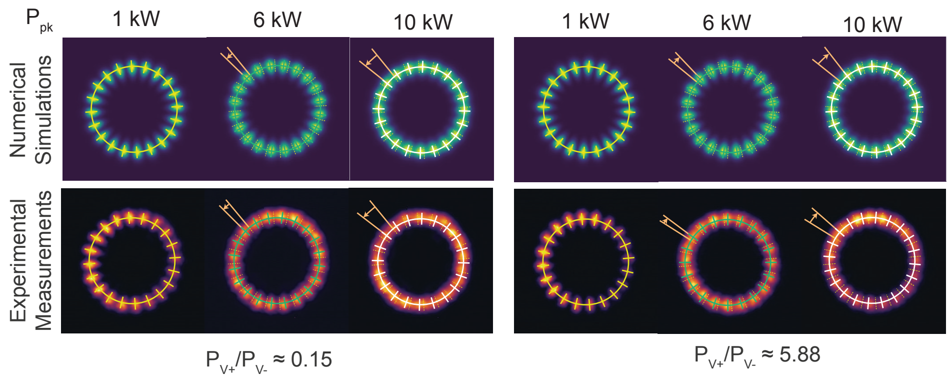

Fig. 5. Nonlinear rotation of unequal superpositions of the $l = \pm 10$ SO_{aa} modes: numerical simulation and experimental images of the time-averaged output intensity pattern imaged through a linear polarizer, at various input peak powers, for two values of mode power ratios P_{V+}/P_{V-}. For visual aid, a wheel pattern is aligned with the lobes and overlaid on top of the images. Notice that the wheel patterns at the different power levels are not aligned with each other, indicating a power-dependent rotation. Also note the opposite sense of rotation in the dominant $l = -10$ case vs the dominant $l = +10$ case.

agreement with numerical simulations shown in Fig. 5 and Supplementary Video 2.

4.3. Image processing and Fourier analysis

To quantitatively analyze the mode rotation from the measured spatial images, we employed Fourier analysis of the azimuthal intensity distributions. As Fig. 6(a) illustrates, we extract the azimuthal variation of intensity along a thin ring concentric within the lobe pattern. Fourier filtering is performed to retain only the 0^{th} and $\pm 20^{th}$ order components, as we are interested in the rotation of the $2|l|$ lobe pattern. The plot in Fig. 6(a) shows that the filtering process retains most of the signal and filters out image distortions and noise caused by uneven illumination, imperfect alignment of imaging optics and potential power leaked into undesired modes because of imperfect input alignment. The rotation of the time-averaged lobe pattern, denoted by δ, is measured using the Fourier phase ζ of the azimuthal intensity signal as $\delta = 18°\zeta/(2\pi)$. A 2π change in azimuthal Fourier phase corresponds to the rotation of the lobe pattern by one full lobe, i.e. $360°/20 = 18°$. The contrast of the lobe patterns (i.e., smearing out) is quantified as the ratio of magnitudes of Fourier amplitudes of the 0^{th} and 20^{th} order components.

The error bars displayed in the experimental data shown in Figs. 6(b) and 6(c) correspond to one standard deviation of observed pattern rotation and lobe contrast based upon collecting 10 time-averaged images for each data point. The sources of error this accounts for includes imaging distortions such as non-uniformity in illumination resulting from imperfect alignment of imaging optics, pulse-to-pulse energy fluctuations in the source laser, as well as errors from the image processing algorithm. These margins of error are in agreement with variation in estimated lobe contrast and pattern rotation upon artificially adding distortions and additive white Gaussian noise to simulated (i.e., otherwise clean) lobe patterns.

The results presented in Fig. 5 are echoed by the plot of lobe pattern rotation as a function of input power shown in Fig. 6(b). In addition to the two cases of unequally excited modes presented in Fig. 5, we also show an additional case (in blue) for which the $l = -10$ mode is dominant, only this time with a different ratio of powers. Fig. 6(b) shows that for all three cases, the amount of rotation experienced by the lobe pattern increases as a function of input power. It

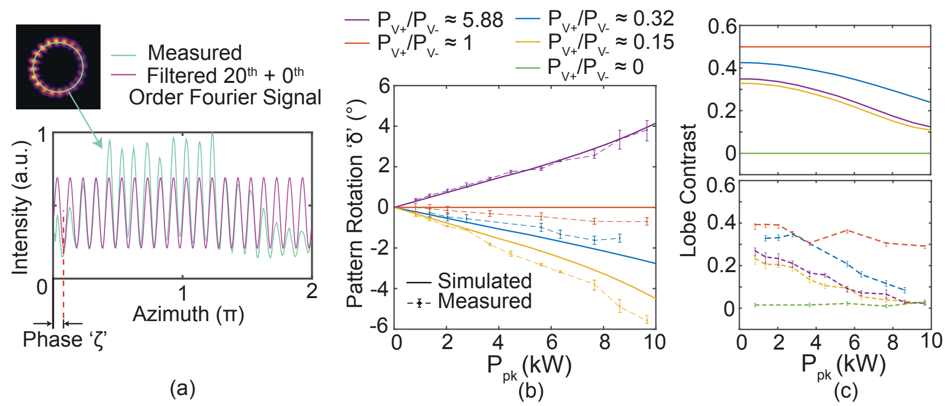

Fig. 6. Fourier analysis of nonlinear rotation via image processing. (a) Illustrative example showing the image processing routine. The intensity pattern along a thin circular ring concentric with the lobe pattern is extracted from the recorded images, and Fourier filtering is performed to retain only the $2|l|^{\text{th}}$ and 0^{th} order components. The rotation of the lobes δ is recovered from the change in Fourier phase ζ of the azimuthal intensity signal with a change in input peak power. The lobe contrast is defined as the magnitude ratio of the 20^{th} and 0^{th} order Fourier components. (b) Rotation δ of the time-averaged lobe pattern at various input powers, for simulation (solid line plots) and experiment (dotted line plots). The plot also shows the control cases of input SOP being circular and linear. (c) Simulated (top; solid line plots) and experimentally measured (bottom; dotted line plots) reduction in lobe contrast as a function of input power.

also shows that the dominant $l = \pm 10$ cases exhibit opposite senses of rotation. Simulations are in agreement with experimental measurements for all three cases. We also show the control case of exciting an equal combination of the two OAM modes, i.e., exciting a pure EH mode. We observe that the lobe pattern in this case exhibits a very small rotation, albeit not perfectly zero, which can be explained by imperfect input coupling causing the two OAM modes to have slightly different powers.

As mentioned before, the reduction in lobe contrast observed in the images of 5 and Supplementary Videos 2, 3 and 4 is a result of temporal averaging over the pulse duration. Fig. 6(c) shows a plot of the lobe contrast, defined as the ratio between the magnitudes of Fourier amplitudes of the 0^{th} and 20^{th} Fourier components. The bottom (dotted line) plot in Fig. 6(c) shows that with an increase in input peak power, we see a reduction in lobe contrast for all three cases of unequal mode excitation, as expected. For the cases of $P_{V+}/P_{V-} \approx 5.88$ and $P_{V+}/P_{V-} \approx 0.15$, though they correspond to cases of dominant $l = +10$ and $l = -10$ respectively, the ratio of powers in the non-dominant mode to the dominant one is approximately equal ($1/5.88 = 0.17$ and 0.15 respectively) in both cases. This explains the near overlap of the two lobe contrast curves in Fig. 6(c) even though the senses of rotation for the two cases are opposite, as shown in Fig. 6(b). For the case of $P_{V+}/P_{V-} \approx 0.32$, because the dominant mode in this case has approximately half the power as the prior two cases, the lobes are expected to have a higher contrast. This explains why the blue curve in Fig 6(c) lies above the curves for the two cases of approximately equal non-dominant to dominant mode power ratio.

This is also in line with the general trend that for an equal excitation of the two OAM modes, the resulting mode in the fiber is a pure EH mode that has spatially-varying *linear* SOP, which produces the best contrast in lobes when imaged through a linear polarizer at low input powers. The unequal excitation cases produce lower lobe contrasts as the spatial profile in the fiber consists of spatially-varying *elliptical* (and not linear) SOP. In the other limiting case of exciting purely one OAM mode, because the SOP is uniformly circular across the entire spatial mode, no lobes are observed even upon the insertion of a linear polarizer at any input power, as shown in Fig. 4 and in the green plots in Fig. 6(c). The trends in the experimentally observed reduction in lobe contrast are in agreement with the numerically simulated values, as shown in the bottom and top plot windows in Fig. 6(c) respectively.

Figs. 6(b) and 6(c) together demonstrate that power-dependent rotation of a spin-orbit coupled state formed by the superposition of two degenerate SO_{aa} modes occurs as a result of intermodal nonlinear interactions between the modes as described in Section 2. Although analogous to nonlinear polarization rotation, this phenomenon is reliant upon the difference in variation of phase across the spatial extent of the fiber modes. To demonstrate this point, consider two modes that have identical phase profiles but opposite helicities of circular polarization. An example of such a mode combination would be the $l = 0$ modes in the hollow RCF used in this work. An unequal superposition of such modes would lead to a spatially uniform elliptical SOP. Insertion of a linear polarizer would not then cause the appearance of a lobe intensity pattern, and a power-dependent rotation of the elliptical SOP in such a case would be completely identical to that occurring in SMFs.

For a mode combination consisting of $|l| > 0$ modes however, such as the combination of $l = \pm 10$ the modes considered here, the phase difference between the modes is spatially variant. It is this spatial variation in phase difference that causes a spatially variant elliptical SOP and thereby the power-dependence of lobes when imaged through a linear polarizer. The nonlinear effect reported here is therefore a generalization of nonlinear polarization rotation occurring in SMFs in the context of spatial OAM modes in fibers.

5. Conclusions

Spatial modes of a hollow RCF of a given topological charge and radial mode order are degenerate with each other depending upon the relative alignment of their OAM and SAM. This results from the so called spin-orbit coupling known to occur in these fibers, where the effective index of a mode of a given topological charge l depends upon its SAM. When two modes of a degenerate group, such as the ${SO_{aa}}^{\pm 10}$ modes described in this work, are excited with unequal amplitudes, the resulting superposition consists of a spatially-varying elliptical SOP. The orientation of this spatial pattern depends upon the phase with which the two modes spatially interfere.

In the presence of optical nonlinearity, the two modes undergo SPM and intermodal XPM. Because of the difference in amplitudes, the nonlinear phases acquired by the two modes are different, and therefore, there is a power-dependent phase difference between the modes. As a result, the spatially-varying elliptical SOP exhibits a power-dependent rotation. This is observed by imaging the lobe pattern caused by passing the beam exiting the fiber through a linear polarizer. This effect constitutes a generalization of the nonlinear polarization rotation effect occurring in SMFs in the context of spatial OAM modes in fibers, and is only observable for OAM modes with $|l| > 0$.

The use of dielectric metasurfaces can further enable introduction of a rich library of spin-orbital coupling effects in the context of nonlinear fiber optics [51], while providing a high-damage threshold platform required for manipulation of high-energy optical pulses. In this work, we report excitation of the desired combination of modes by using a transmissive dielectric metasurface q-plate. We observe the nonlinear rotation by imaging the time-averaged intensity through a linear polarizer as a function of input power. We observe a clear dependence of the orientation of the spatial pattern on input power. Notably, the sense of rotation is opposite for cases of a dominant $l = +10$ and dominant $l = -10$ SO_{aa} modes, in strong agreement with analytical predictions and numerical simulation. At higher input powers, time-dependent nonlinear rotation of the lobe pattern occurs within one pulse duration, leading to a spatial blurring of the observed lobe pattern. In conclusion, we report the first to our knowledge observation of the spatial OAM generalization of the well known nonlinear polarization rotation effect.

The measurements reported here also constitute the first observations, to our knowledge, of the effects of SPM and XPM on co-propagating OAM modes in fibers, which is of fundamental interest in applications ranging from OAM-based classical and quantum communication to quantum optics and particle trapping.

References

1. L. Allen, M. W. Beijersbergen, R. J. C. Spreeuw, and J. P. Woerdman, "Orbital angular momentum of light and the transformation of laguerre-gaussian laser modes," Phys. Rev. A **45**, 8185 (1992).
2. A. Ashkin, "Acceleration and trapping of particles by radiation pressure," Phys. Rev. Lett. **24**, 156 (1970).
3. D. G. Grier, "A revolution in optical manipulation," Nature **424**, 810–816 (2003).
4. Y. Yang, Y. X. Ren, M. Chen, Y. Arita, and C. Rosales-Guzmán, "Optical trapping with structured light: a review," Adv. Photonics **3**, 034001 (2021).
5. N. Bozinovic, Y. Yue, Y. Ren, M. Tur, P. Kristensen, H. Huang, A. E. Willner, and S. Ramachandran, "Terabit-scale orbital angular momentum mode division multiplexing in fibers," Science **340**, 1545–1548 (2013).
6. J. Wang, J. Y. Yang, I. M. Fazal, N. Ahmed, Y. Yan, H. Huang, Y. Ren, Y. Yue, S. Dolinar, M. Tur, and A. E. Willner, "Terabit free-space data transmission employing orbital angular momentum multiplexing," Nat. Photonics **6**, 488–496 (2012).
7. B. Ung, P. Vaity, L. Wang, Y. Messaddeq, L. A. Rusch, and S. LaRochelle, "Few-mode fiber with inverse-parabolic graded-index profile for transmission of oam-carrying modes," Opt. Express **22**, 18044–18055 (2014).
8. F. Zhang, K. Zou, Y. Zhu, and Z. Zheng, "1.44 tb/s free-space im-dd transmission employing oam multiplexing and pdm," Opt. Express **24**, 3967–3980 (2016).
9. A. Mair, A. Vaziri, G. Weihs, and A. Zeilinger, "Entanglement of the orbital angular momentum states of photons," Nat. 2001 412:6844 **412**, 313–316 (2001).
10. L. Marrucci, E. Karimi, S. Slussarenko, B. Piccirillo, E. Santamato, E. Nagali, and F. Sciarrino, "Spin-to-orbital conversion of the angular momentum of light and its classical and quantum applications," J. Opt. **13**, 064001 (2011).
11. D. Bacco, D. Cozzolino, B. D. Lio, Y. Ding, K. Rottwitt, and L. K. Oxenlowe, "Quantum communication with orbital angular momentum," Int. Conf. on Transparent Opt. Networks (2020).
12. A. Belmonte, C. Rosales-Guzmán, and J. P. Torres, "Measurement of flow vorticity with helical beams of light," Optica **2**, 1002–1005 (2015).
13. E. Otte and C. Denz, "Optical trapping gets structure: Structured light for advanced optical manipulation," Appl. Phys. Rev. **7**, 41308 (2020).
14. M. Krenn, M. Malik, M. Erhard, and A. Zeilinger, "Orbital angular momentum of photons and the entanglement of laguerre–gaussian modes," Philos. transactions. Ser. A, Math. physical, engineering sciences **375** (2017).
15. R. Fickler, G. Campbell, B. Buchler, P. K. Lam, and A. Zeilinger, "Quantum entanglement of angular momentum states with quantum numbers up to 10,010," Proc. Natl. Acad. Sci. United States Am. **113**, 13642–13647 (2016).
16. J. Leach, B. Jack, J. Romero, A. K. Jha, A. M. Yao, S. Franke-Arnold, D. G. Ireland, R. W. Boyd, S. M. Barnett, and M. J. Padgett, "Quantum correlations in optical angle-orbital angular momentum variables," Science **329**, 662–665 (2010).
17. C. Brunet, P. Vaity, Y. Messaddeq, S. LaRochelle, and L. A. Rusch, "Design, fabrication and validation of an oam fiber supporting 36 states," Opt. Express **22**, 26117–26127 (2014).
18. P. Gregg, P. Kristensen, and S. Ramachandran, "Conservation of orbital angular momentum in air-core optical fibers," Optica **2**, 267–270 (2015).
19. R. Essiambre, G. Kramer, P. J. Winzer, G. J. Foschini, and B. Goebel, "Capacity limits of optical fiber networks," J. Light. Technol. **28**, 662–701 (2010).
20. R.-J. Essiambre, R. Tkach, and R. Ryf, *Fiber Nonlinearity and Capacity: Single-Mode and Multimode Fibers* (Elsevier, 2013), pp. 1–43.
21. P. Mitra and J. Stark, "Nonlinear limits to the information capacity of optical fibre communications," Nature **411**, 1027–1030 (2001).
22. Z. Liu, L. G. Wright, D. N. Christodoulides, and F. W. Wise, "Kerr self-cleaning of femtosecond-pulsed beams in graded-index multimode fiber," Opt. Lett. **41**, 3675–3678 (2016).
23. K. Krupa, A. Tonello, B. M. Shalaby, M. Fabert, A. Barthélémy, G. Millot, S. Wabnitz, and V. Couderc, "Spatial beam self-cleaning in multimode fibres," Nat. Photon. **11**, 237–241 (2017).
24. W. H. Renninger and F. W. Wise, "Optical solitons in graded-index multimode fibres," Nat. Commun. **4**, 1719 (2013).
25. K. Krupa, A. Tonello, A. Barthélémy, V. Couderc, B. M. Shalaby, A. Bendahmane, G. Millot, and S. Wabnitz, "Observation of Geometric Parametric Instability Induced by the Periodic Spatial Self-Imaging of Multimode Waves," Phys. Rev. Lett. **116**, 183901 (2016).
26. M. A. Eftekhar, L. G. Wright, M. S. Mills, M. Kolesik, R. A. Correa, F. W. Wise, and D. N. Christodoulides, "Versatile supercontinuum generation in parabolic multimode optical fibers," Opt. Express **25**, 9078–9087 (2017).

27. L. G. Wright, Z. Liu, D. A. Nolan, M.-J. Li, D. N. Christodoulides, and F. W. Wise, "Self-organized instability in graded-index multimode fibres," Nat. Photon. **10**, 771–776 (2016).
28. G. Prabhakar, L. Rishoj, P. Gregg, P. Kristensen, and S. Ramachandran, "Octave-wide supercontinuum generation of light-carrying orbital angular momentum," Opt. Express **27**, 11547–11556 (2019).
29. L. Yan, P. Kristensen, and S. Ramachandran, "Vortex fibers for sted microscopy," APL Photonics **4**, 022903 (2018).
30. X. Liu, E. N. Christensen, K. Rottwitt, and S. Ramachandran, "Nonlinear four-wave mixing with enhanced diversity and selectivity via spin and orbital angular momentum conservation," APL Photonics **5**, 010802 (2020).
31. S. Ramachandran, P. Gregg, P. Kristensen, and S. E. Golowich, "On the scalability of ring fiber designs for oam multiplexing," Opt. Express **23**, 3721–3730 (2015).
32. M. J. Padgett, S. Ramachandran, S. D. Johnson, and Z. Ma, "Measurement of the spin-orbit coupling interaction in ring-core optical fibers," OSA Continuum **2**, 2975–2982 (2019).
33. P. Gregg, P. Kristensen, A. Rubano, S. Golowich, L. Marrucci, and S. Ramachandran, "Enhanced spin orbit interaction of light in highly confining optical fibers for mode division multiplexing," Nat. Commun. **10**, 1–8 (2019).
34. S. S. Oemrawsingh, J. A. V. Houwelingen, E. R. Eliel, J. P. Woerdman, E. J. Verstegen, J. G. Kloosterboer, and G. W. T. Hooft, "Production and characterization of spiral phase plates for optical wavelengths," Appl. Opt. **43**, 688–694 (2004).
35. M. W. Beijersbergen, L. Allen, H. E. van der Veen, and J. P. Woerdman, "Astigmatic laser mode converters and transfer of orbital angular momentum," Opt. Commun. **96**, 123–132 (1993).
36. V. Y. Bazhenov, M. S. Soskin, and M. V. Vasnetsov, "Screw dislocations in light wavefronts," J. Mod. Opt. **39**, 985–990 (1992).
37. A. Rubano, B. Piccirillo, F. Cardano, and L. Marrucci, "Q-plate technology: a progress review [invited]," JOSA B **36**, D70–D87 (2019).
38. R. C. Devlin, A. Ambrosio, N. A. Rubin, J. P. B. Mueller, and F. Capasso, "Arbitrary spin-to–orbital angular momentum conversion of light," Science **358**, 896–901 (2017).
39. M. Piccardo and A. Ambrosio, "Arbitrary polarization conversion for pure vortex generation with a single metasurface," Nanophotonics **10**, 727–732 (2020).
40. W. Ji, C. H. Lee, P. Chen, W. Hu, Y. Ming, L. Zhang, T. H. Lin, V. Chigrinov, and Y. Q. Lu, "Meta-q-plate for complex beam shaping," Sci. Reports **6**, 1–7 (2016).
41. S. Kruk, B. Hopkins, I. I. Kravchenko, A. Miroshnichenko, D. N. Neshev, and Y. S. Kivshar, "Invited article: Broadband highly efficient dielectric metadevices for polarization control," APL Photonics **1**, 030801 (2016).
42. C. Antonelli, M. Shtaif, and A. Mecozzi, "Modeling of nonlinear propagation in space-division multiplexed fiber-optic transmission," J. Light. Technol. **34**, 36–54 (2016).
43. G. Agrawal, "Nonlinear fiber optics," Fifth Ed. (2012).
44. A. Fallahkhair, K. S. Li, and T. E. Murphy, "Vector finite difference modesolver for anisotropic dielectric waveguides," J. Light. Technol. **26**, 1423–1431 (2008).
45. W. R. McGehee, W. Zhu, D. S. Barker, D. Westly, A. Yulaev, N. Klimov, A. Agrawal, S. Eckel, V. Aksyuk, and J. J. McClelland, "Magneto-optical trapping using planar optics," New J. Phys. **23**, 013021 (2021).
46. M. Khorasaninejad, W. T. Chen, R. C. Devlin, J. Oh, A. Y. Zhu, and F. Capasso, "Metalenses at visible wavelengths: Diffraction-limited focusing and subwavelength resolution imaging," Science **352**, 1190–1194 (2016).
47. S. Shrestha, A. C. Overvig, M. Lu, A. Stein, and N. Yu, "Broadband achromatic dielectric metalenses," Light. Sci. & Appl. 2018 7:1 **7**, 1–11 (2018).
48. R. L. Phillips and L. C. Andrews, "Spot size and divergence for laguerre gaussian beams of any order," Appl. Opt. **22**, 643–644 (1983).
49. S. K. Dacha and T. E. Murphy, "Spatiotemporal characterization of nonlinear intermodal interference between selectively excited modes of a few-mode fiber," Optica **7**, 1796–1803 (2020).
50. Y. Leventoux, G. Granger, K. Krupa, A. Tonello, G. Millot, M. Ferraro, F. Mangini, M. Zitelli, S. Wabnitz, S. Février, and V. Couderc, "3d time-domain beam mapping for studying nonlinear dynamics in multimode optical fibers," Opt. Lett. **46**, 66–69 (2021).
51. S. Xiao, J. Wang, F. Liu, S. Zhang, X. Yin, and J. Li, "Spin-dependent optics with metasurfaces," Nanophotonics **6**, 215–234 (2017).